An Experimental and Theoretical Study of Glycerol Oxidation to 1,3-Dihydroxyacetone over Bimetallic Pt-Bi Catalysts

Yang Xiao, Jeffrey Greeley, and Arvind Varma
School of Chemical Engineering, Purdue University, West Lafayette, IN 47907-2100

Zhi-Jian Zhao
School of Chemical Engineering, Purdue University, West Lafayette, IN 47907-2100

Key Laboratory for Green Chemical Technology of Ministry of Education, School of Chemical Engineering and Technology, Tianjin University, Collaborative Innovation Center of Chemical Science and Engineering, Tianjin 300072, P.R. China

Guomin Xiao
School of Chemistry and Chemical Engineering, Southeast University, Nanjing 211189, P.R. China

DOI 10.1002/aic.15418
Published online July 25, 2016 in Wiley Online Library (wileyonlinelibrary.com)

It is important to utilize glycerol, the main by-product of biodiesel, to manufacture value-added chemicals such as 1,3-dihydroxyacetone (DHA). In the present work, the performance of five different catalysts (Pt-Bi/AC, Pt-Bi/ZSM-5, Pt/MCM-41, Pt-Bi/MCM-41, and Pt/Bi-doped-MCM-41) was investigated experimentally, where Pt-Bi/MCM-41 was found to exhibit the highest DHA yield. To better understand the experimental results and to obtain insight into the reaction mechanism, density functional theory (DFT) computations were conducted to provide energy barriers of elementary steps. Both experimental and calculated results show that for high DHA selectivity, Bi should be located in an adatom-like configuration Pt, rather than inside Pt. A favorable pathway and catalytic cycle of DHA formation were proposed based on the DFT results. A cooperative effect, between Pt as the primary component and Bi as a promoter, was identified for DHA formation. Both experimental and theoretical considerations demonstrate that Pt-Bi is efficient to convert glycerol to DHA selectively. © 2016 American Institute of Chemical Engineers *AIChE J*, 63: 705–715, 2017
Keywords: biodiesel, glycerol selective oxidation, pt-bi catalyst, dft, 1,3-dihydroxyacetone

Introduction

Biodiesel, a common biofuel, has been of increasing importance in recent years owing to the emphasis on sustainable fuels production. It is produced by transesterification and/or esterification between triglycerides (vegetable oils, animal fats, waste oils, etc.) and short chain alcohols, typically methanol or ethanol, catalyzed by acid, alkali or enzyme catalysts.[1,2] All biodiesel production technologies generate surplus crude glycerol as the primary by-product, which has low value. The purification and utilization of crude glycerol is important to enhance economics of the biodiesel process.[3] High-value added uses for glycerol include animal feedstock, cosmetics, pharmaceuticals, and chemical intermediates such as 1,3-propanediol, succinic acid, and 1,3-dihydroxyacetone (DHA).[4]

DHA is an important chemical used as a sunless tanning agent in the cosmetics industry, in winemaking, and as a chemical intermediate in pharmaceutical and organic synthesis fields. Owing to higher DHA selectivity, fermentation is currently preferentially employed over conventional catalytic processes to manufacture DHA. Catalytic processes, however, offer higher reaction rates, hence productivity, giving motivation to develop such routes for DHA production. Platinum (Pt), as a noble transition metal, is among the most efficient oxidation catalysts.[5] Platinum alone, however, preferentially oxidizes the primary hydroxyl group of glycerol,[6] whereas DHA arises from the secondary hydroxyl group oxidation. Kimura et al.[7] proposed a platinum-bismuth (Pt-Bi) bimetallic catalyst to selectively oxidize the secondary hydroxyl group to produce DHA in a batch reactor, and DHA yield was further increased using a fixed-bed reactor.[8]

In general, knowledge of heterogeneous catalytic mechanism is important to optimize active species distribution on supports, acquire multi-scale micro- and macro-kinetic data, screen metal candidates, and design an effective catalyst for a given reaction.[9,10] For selective oxidation of glycerol on Pt-Bi catalysts, it was postulated that bismuth adatoms function as site blockers on Pt (111), controlling glycerol orientation and leading to DHA formation.[7,8] Using density functional theory (DFT) calculations, Kapur et al.[11] proposed that for CO oxidation the bismuth promoter functions through both electronic and geometric effects, decreasing the reaction barrier significantly. It was suggested that gaseous O_2 may react with

Additional Supporting Information may be found in the online version of this article.

Correspondence concerning this article should be addressed to A. Varma at avarma@purdue.edu.

© 2016 American Institute of Chemical Engineers

surface bismuth to form new active sites, changing the status of Bi, which may play an important role in selective oxidation.[12] This suggestion, however, was questioned, as a rate-determining step was found to be zero order in oxygen.[13] Thus, it is of interest to determine the role of bismuth in glycerol selective oxidation to DHA.

Noble metals used as active species for catalytic conversion are generally dispersed on supports, typically with high surface area and porous structure. Activated carbon (AC) is one such support, although its pore structure and pore size distribution are not ordered, and its mechanical strength is low. ZSM-5 is an important member of the zeolite family and widely used as a support for numerous petrochemical applications.[14–16] The micro-pore size (0.2–2 nm) and shape selectivity of ZSM-5, however, restrict applications for components with large size molecules such as glycerol (diameter ~0.5 nm). MCM-41, by contrast, is a mesoporous (pore size 2–50 nm) molecular sieve support that displays larger pore size, long-range order, high surface area, and good thermal stability.[17,18] In addition, modification of these materials by ion exchange, heteroatom substitution, channel, and surface structure property improvement gives the potential to exhibit high activity for specific reactions. Heteroatom substitution of silica or alumina in the framework structures of molecular sieves, known as metal doping, forms alkaline-acidic sites or redox sites capable of catalyzing redox reactions,[19,20] and this approach is followed in the present work.

In our previous work, a series of optimized Pt-Bi catalysts was prepared for glycerol selective oxidation to DHA,[21] and a kinetic network model was developed to describe the dynamic behavior.[22] In the present work, activity and kinetics of Pt-Bi/AC, Pt-Bi/ZSM-5, Pt/MCM-41, Pt-Bi/MCM-41, and Pt/Bi-doped MCM-41 are investigated. DFT calculations are conducted to obtain energy barriers of elementary steps and reaction pathways,[23–25] and to elucidate the effect of Bi as an additive to Pt catalysts.

Experimental

Materials

Product Analysis

Chloroplatinic acid hydrate (99.9% metal basis) and bismuth chloride (99.999%) were used as metal precursors, both from Sigma Aldrich, as were cetyl pyridine bromide (CPBr) and ZSM-5. The activated carbon was Darco granular 20–40 mesh from Norit Americas Inc. The following chemicals were obtained from Alfa Aesar: pure glycerol, sodium borohydride (SBH) stable aqueous solution (4.4 M in 14 M sodiumhydroxide), tetramethylammonium hydroxide (TMAH, 25%wt in aqueous solution), hexadecyltrimethylammonium bromide (CTAB) and tetraethoxysilane (TEOS). Hydrochloric acid solution (37 wt %), sodium hydroxide pellets, both ACS grade, were from Mallinckrodt Chemicals. Ultra-high purity grade gases (99.999% helium, 99.92% oxygen and 99.999% H_2) were purchased from Indiana Oxygen. The $0.5\%Pt/Al_2O_3$ (metal dispersion = 31 ± 0.5%) standard used for chemisorption calibration was obtained from Micromeritics.

Compositions of glycerol and DHA in reaction samples were quantitatively analyzed by a gas chromatograph (Agilent GC 5890) equipped with a flame ionization detector and a Select Biodiesel for glycerides ultiMetal Column (15 m, 0.32 mm, 0.10μm) with a retention gap. TMAH was used as a derivatization reagent to decrease the volatility of glycerol and DHA. Helium was used as the carrier gas with a constant flow rate of 3.0 mL/min and a split ratio of 100. The temperatures of the injector and the detector were 300 and 380°C, respectively. The GC oven employed a temperature program as follows: 50°C (maintained for 1 min), to 60°C at 1°C/min, to 300°C at 10°C/min, and finally to 380°C at 30°C/min (maintained for 10 min).

Catalyst Preparation

Pt and Bi were loaded on AC sequentially, following our prior work, to obtain 3% Pt–0.6% Bi/AC catalyst, where the loadings were by weight. Briefly, Pt and Bi were loaded using the sequential wet impregnation method with Pt loaded first, followed by Bi. The Pt and Bi precursors were dissolved separately in 1.2 mol/L HCl, and then added dropwise sequentially to the well-stirred AC slurry, with stirring continued for at least 8 h at room temperature for each metal loading. The slurry was then rinsed, dried in air at 100°C and reduced using SBH before use. More details are available in our prior work.[21] The 3% Pt–0.6% Bi/ZSM-5 catalyst was prepared by the same procedure, with the only difference that AC support was replaced by ZSM-5 support. Only 3% Pt–0.6% Bi catalysts were investigated in the present work, because such composition was found to exhibit the highest yield of DHA.[21]

To prepare the MCM-41 based catalyst, silica-based MCM-41 support was synthesized first using a procedure similar to that described previously.[26,27] This was accomplished by the hydrothermal method in a Parr Large Capacity Acid Digestion Vessel (Model 4748, 150 mL) with PTFE-lining. The molar ratio of CTAB : Si : H_2O was 0.2:1:70. Measured TEOS solution was added dropwise to CTAB (templating agent) solution in a beaker under vigorous stirring, followed by adjusting pH to 10.5 through gradual addition of 1 M NaOH solution. The solution was then stirred at 353 K for 80 min. The sol-gel was transferred to the Parr vessel and kept under an isothermal environment at 383 K for 48 h. Once cooled to room temperature, solids were separated by vacuum filtration, followed by rinsing with deionized water and dried for 4 h. The templating agent was removed by calcination of the MCM-41 precursor in air at 823 K for 6 h. Subsequently, both 3% Pt/MCM-41 and 3% Pt–0.6% Bi/MCM-41 catalysts were prepared by the same procedure as described before.[21]

For bismuth doped MCM-41 support synthesis, CPBr was used as the templating agent instead of CTAB. The molar ratio of the reagents were CPBr : TEOS : HCl : H_2O : Bi = 0.33:1:7.5:68:0.07. After the Bi-MCM-41 precursor was prepared, the same post-pretreatment procedure was conducted as for silica-based MCM-41. Following this, Pt was loaded on Bi-MCM-41 to obtain 3% Pt/Bi-MCM-41 catalyst.

As noted above, the Pt and Bi loadings in all cases where the metals are placed on the support, were 3 and 0.6 wt %, respectively. For this reason, in later sections the metal loadings are not noted explicitly when describing the catalysts. Thus, e.g., Pt-Bi/MCM-41 refers to 3 wt % Pt and 0.6 wt % Bi placed on MCM-41 support. For the case where Bi is incorporated in the MCM-41 skeletal structure, similarly, Pt/Bi-MCM-41 refers to 3 wt % Pt placed on the 0.6 wt % Bi-doped MCM-41 support.

Catalyst Characterization

The physisorption properties of the catalysts, including BET surface area, pore size distribution, average pore volume and pore diameter, were measured using a Micromeritics

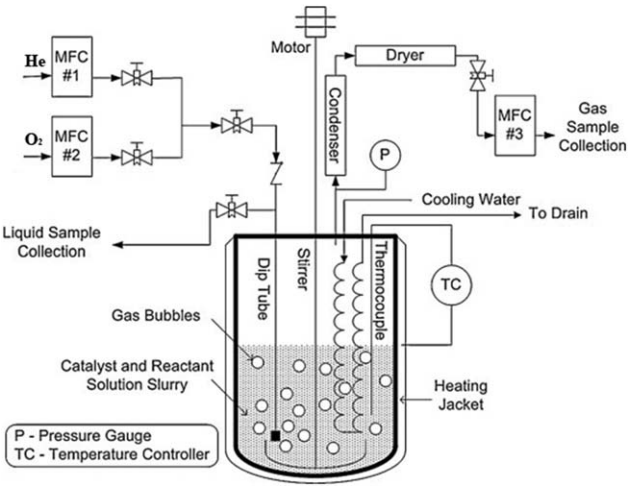


Figure 1. Pressure semi-batch reactor system.

ASAP 2000 apparatus, where nitrogen was used as adsorbent gas. Degassing was performed at 280°C for 6 h before measurements. The Pt dispersion was obtained using the H_2–O_2 titration approach,[28] where the calibration was done using the 0.5% Pt/Al_2O_3 standard described in "Materials" section. The surface morphology of catalyst samples was obtained using a FEI-Tecnai transmission electron microscope (TEM), operated at 200 kV with LaB_6 source. The samples were prepared by suspending the catalyst particles in water, collecting the fines, and placing them on a 200 copper mesh with lacey carbon film coating, followed by drying in air.

Glycerol Selective Oxidation Tests

The reaction experiments were performed in a high pressure reactor from Parr Instrument Company (model 4561 series), shown in Figure 1. A 10 μm porous frit was used at the end of the dip tube for gas dispersion in the liquid solution, and also functioned as a filter when collecting liquid samples. The reactions were conducted at 75°C and 30 psig O_2. The experimental procedure was as follows. First, the reactor was charged with 5.0 g catalyst and 175 mL 1.0 M glycerol solution. The reactor was purged with helium for 10 min before the temperature controller was turned on. After reaching the desired temperature, the gas was switched to O_2, which flowed through the reactor continuously at 400 sccm controlled with a MFC. Liquid samples were collected every 15 min in the first hour and subsequently every 30 min for the 5-h reaction period.

DFT Calculations

The periodic plane-wave-based code Vienna Ab-initio Simulation Package,[29,30] was used for all the DFT calculations, employing the projector augmented wave,[31,32] method for ionic cores and the PW91[33] form of exchange-correlation functional in the generalized-gradient approximation. In all cases, a cutoff energy of 400 eV was applied for the plane wave basis, while a first-order Methfessel-Paxton smearing with a width of 0.15 eV[34] was employed and the total energies are evaluated by extrapolating to zero broadening. Monkhorst-Pack meshes of $7 \times 7 \times 1$, $5 \times 5 \times 1$, and $3 \times 3 \times 1$ k points were used to sample the surface Brillouin zone,[35] for $p(2 \times 2)$, $p(3 \times 3)$, and $p(4 \times 4)$ unit cells of Pt(111) slabs, respectively. The Γ-point k-point sampling was used for gas phase components, which were placed in a box with dimensions of $18 \times 19 \times 20$ Å. Convergence of binding energies (BE) with respect to all electronic parameters was confirmed. The self-consistent iterations were converged with a criterion of 1×10^{-4} eV, and the ionic steps were converged to 0.02 eV/Å. Dipole corrections were included only in the direction perpendicular to slab surface. Spin polarization was applied for gas phase radicals due to the possible presence of unpaired electrons.

The DFT-determined lattice constant for Pt was found to be 3.98 Å, which agrees well with the experimental bulk lattice constant (3.92 Å)[36]; this lattice value is also consistent with other lattice constants reported in the literature for Pt.[37–39] Four-layer slab models were employed to model the Pt(111) surfaces in a super-cell geometry with 1.2 nm vacuum spacing between them. During the geometry optimization, only the top two layers with the adsorbates were allowed to relax, while the other two layers were fixed according to bulk-terminated geometry. Test calculations showed that the BE and barriers were converged to <0.01 eV when the top three layers were relaxed.

The dimer[40] and/or climbing-image nudged elastic band method,[41,42] was used to locate the structures of transition states (TS) in the reactions. Each transition state was confirmed to have only one imaginary vibrational mode by vibrational normal mode analysis. Note that various possible initial states were considered for energy barrier calculations, while only the lowest barrier was used in the analysis on the reaction kinetics and selectivity. The BE of adsorbates and reaction barriers for given reactions were determined by Eqs. 1 and 2.

$$\mathrm{BE} = \mathrm{E}_{ad/slab} - \mathrm{E}_{ad} - \mathrm{E}_{slab} \quad (1)$$

$$\mathrm{E}_a = E_{TS} - E_{IS} \quad (2)$$

A negative value of BE implies an exothermic process or a favorable interaction, while a positive value of the BE means an endothermic process or an unfavorable interaction. Reaction energies/barriers were calculated using Gibbs free energies obtained from the DFT formation energy plus zero-point energy and finite-temperature entropy corrections. For gas phase species, the vibrational, translational, and rotational modes were included for entropy corrections. For an adsorbed intermediate, the translational and rotational modes were replaced by vibrational modes corresponding to frustrated translation and rotation on the surface.[43,44]

Since bismuth could be oxidized in the environment of oxygen (partial pressure = 30 psig at ~350 K in this work), phase diagrams of various oxides of bismuth were obtained by determining the surface free energy of Bi_xO_y-Pt(111) slabs as a function of oxygen chemical potential. In general, for each model, the geometry of an absorbed Bi_xO_y cluster on Pt(111) was optimized by particle swarm optimization,[45] using the CALYPSO code.[46,47] Then, energies of optimized geometries were obtained to calculate the surface free energies, using Eq. 3, wherein the only free variable is the oxygen chemical potential.

Table 1. Characterization for Porous Supports

Material	Specific surface area (m^2/g)	Average pore diameter (nm)
AC	600	4.0
ZSM-5	362	0.4
MCM-41	1025	1.9
Bi-MCM-41	701	2.8

Table 2. Characterization for Metal Supported Catalysts

Materials	Specific surface area (m^2/g)	Average pore diameter (nm)	Pt dispersion (%)	Metal particle size (nm)
Pt-Bi/AC	492	3.7	22.2	4.9
Pt-Bi/ZSM-5	306	0.3	27.6	4.1
Pt-Bi/MCM-41	897	1.9	39.4	2.2
Pt/Bi-MCM-41	635	2.6	33.9	2.3

$$\gamma(T,p)=\frac{1}{A}\left[G^{slab}\left(Bi_xO_y,Pt\right)-G^{slab}(Pt)-\frac{x}{2}g^{bulk}_{Bi_2O_3}+\left(\frac{3}{2}x-y\right)\mu_O\right], \quad (3)$$

$$\mu_{O2}(T,p)=\mu_{O2}\left(T,p^0\right)+kT\ln\left(\frac{p}{p^0}\right), \quad (4)$$

$$\mu_O(T,p)=1/2\mu_{O2}(T,p), \quad (5)$$

where $p^0 = 1$ atm and $G^{slab}\left(Bi_xO_y,Pt\right)$ is the Gibbs free energy of a Bi_xO_y cluster binding on a Pt slab, while $G^{slab}(Pt)$ is the Gibbs free energy of a clean Pt slab. As suggested by experimental conditions, it is preferred to use oxygen chemical potential (μ_O) to discuss the dependence of the surface on the O_2 pressure and temperature. The oxygen-poor limit was determined by decreasing μ_O until the oxide decomposes into solid Bi and gaseous oxygen, while the oxygen-rich limit gas was set by increasing μ_O until gas phase O_2 started to condensate on the sample. Considering μ_O as a function of temperature and oxygen partial pressure, Eqs. 4 and 5 were used to correlate operating conditions with the most stable surface composition and geometry, with respect to minimum surface free energy. For more details related to Eqs. 3–5, please refer to Supporting Information and published papers.[48,49]

Results and Discussion

Catalyst characterization results

The characterization results for the porous supports and supported catalysts are shown in Tables 1 and 2, respectively, where BET method[50] was used to calculate specific areas and average pore diameters. Both the specific surface area and pore diameter values for ZSM-5 and MCM-41 are consistent with those reported in literature.[51–53] Adsorption and desorption isotherms for MCM-41 and Bi-MCM-41 are shown in Figure 2. Based on the classification of adsorption isotherms,[54,55] both curves have the characteristic shape for mesoporous materials. In Table 1, AC and Bi-MCM-41 also have high specific areas, implying high capacities to adsorb reactants. Average pore diameter data in Table 1 illustrates that ZSM-5 is a microporous material (pore diameter <2 nm), while others are mesoporous (2 nm $<$ pore diameter $<$ 50 nm). As shown in Table 2, after metals (Pt and Bi) are loaded on these supports, specific surface areas decrease somewhat, while average pore diameters remain essentially the same. The Pt dispersion (20–40%) and metal particle sizes (2–5 nm) of these supported catalysts are also listed in Table 2, which are consistent with the TEM scan results in Figure 3, and reflect that smaller metal particle sizes lead to higher Pt dispersion.[56] According to the physisorption and TEM results, both synthesized MCM-41 and Bi-MCM-41 supports are mesoporous materials with ordered pore structure and narrow pore size distributions. Note that catalysts loaded on ordered mesoporous supports (Pt-Bi/MCM-41 and Pt/Bi-MCM-41) have higher Pt dispersions than those on microporous (ZSM-5) and amorphous mesoporous supports (AC).

Kinetic behavior of different catalysts

Figure 4 illustrates the kinetic behavior of five different catalysts (Pt-Bi/AC, Pt-Bi/ZSM-5, Pt/MCM-41, Pt-Bi/MCM-41, and Pt/Bi-MCM-41) for glycerol conversion in terms of DHA yield, since DHA is the only product of concern in this work. The profiles of glycerol/product concentrations can be found in Supporting Information Table S1. The corresponding values of the turnover frequencies (TOF) and DHA selectivities are shown in Table 3. The absence of mass transfer limitations (both internal and external diffusion) was confirmed by using the same criteria as in our prior work.[21,22]

We note that two main by-products (glyceric acid and glyceraldehyde (GLA)) are reported in Supporting Information Table S1, while other products are not reported owing to their low amounts ($<2\%$).[21] Further, glyceric acid is easily obtained from further oxidation of GLA.[22,57] GLA is the product of

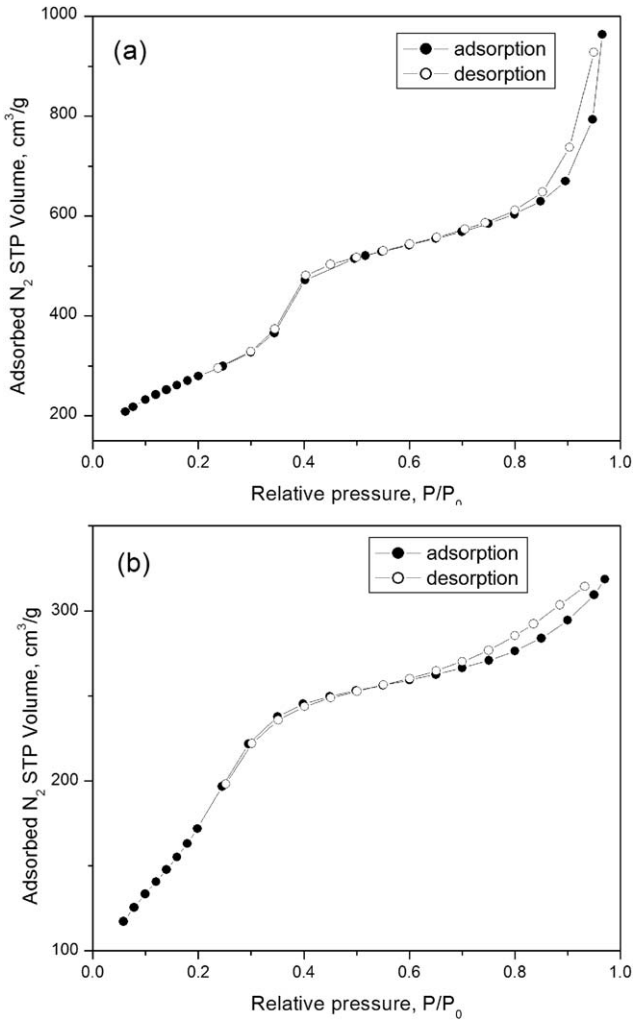


Figure 2. Adsorption and desorption isotherms for (a) MCM-41 and (b) Bi-MCM-41.

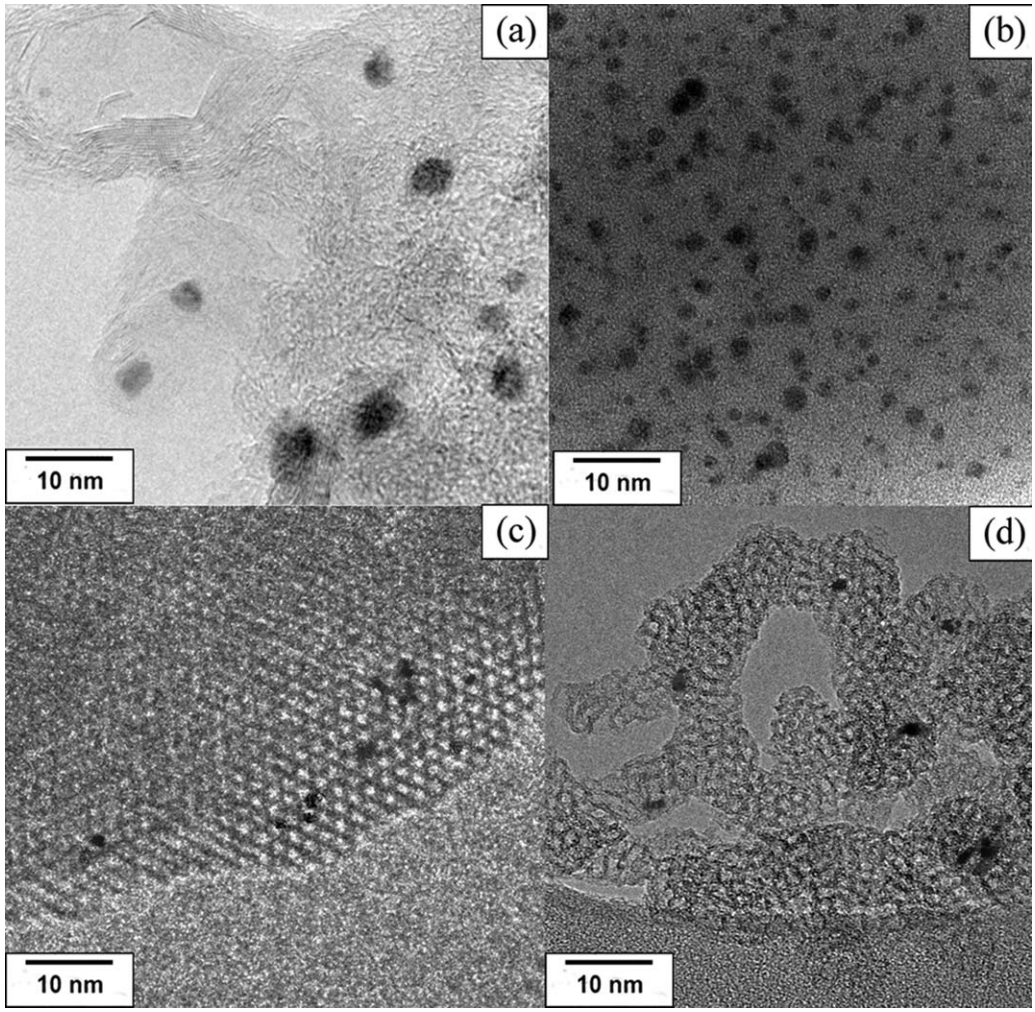


Figure 3. TEM scans for (a) Pt-Bi/AC, (b) Pt-Bi/ZSM-5, (c) Pt-Bi/MCM-41, and (d) Pt/Bi-MCM-41.

primary –OH oxidation from glycerol, while DHA is formed by secondary –OH oxidation of glycerol. Thus, oxidation of secondary or primary –OH of glycerol is the key consideration of whether DHA is formed or not, which is discussed in detail in the section on "mechanism of glycerol selective oxidation".

Several features may be seen from the data in Figure 4 and Table 3. The TOF and DHA selectivity values over Pt-Bi bimetallic catalyst are consistent with our prior work.[21] Pt alone negligibly converts glycerol to DHA, where its observed yields are typically lower than 10%. This agrees with prior literature,[21,58,59] and implies that, along with Pt, the Bi species is required to obtain DHA from glycerol oxidation. Both Pt-Bi/MCM-41 and Pt-Bi/AC gave high DHA yields, while Pt-Bi/ZSM-5 exhibits relatively lower yield of DHA. The differences in kinetic behavior between Pt-Bi/MCM-41 and Pt-Bi/ZSM-5 can be explained by the combined effect of surface area, metal particle and metal dispersion.[60] As shown in Tables 1 and 2, a higher surface area of MCM-41 support may result in a smaller metal particle size and hence a larger metal dispersion. The larger Pt dispersion and higher surface area for the MCM-41 support contribute to the superior performance of the Pt-Bi/MCM-41 catalyst. The kinetic behavior difference between Pt-Bi/MCM-41 and Pt-Bi/AC may be attributed to different surface areas and metal dispersions. The Pt-Bi/MCM-41 catalyst shows ordered structure (uniform parallel channels), higher surface area (897 m^2/g), and Pt dispersion (39.4%), while the Pt-Bi/AC catalyst shows amorphous structure, lower surface area (492 m^2/g), and Pt dispersion (22.2%). A similar feature was also observed in the literature.[61,62]

The difference between Pt-Bi/MCM-41 (Pt and Bi loaded on MCM-41, separately) and Pt/Bi-MCM-41 (Pt loaded on Bi-doped MCM-41) may result from other reasons, since both catalysts have similar pore structures, pore sizes, metal dispersion, and metal particle sizes, as shown in Table 2. The Bi-MCM-41 was reported as an efficient catalyst for liquid-phase oxidation of cyclohexane where Bi functions as an active metal, modifying acidity and pore structure of pure MCM-41.[63] This is not true, however, in the selective oxidation of glycerol to DHA, according to the kinetic results in Figure 4. The main difference between Pt/Bi-MCM-41 and other Pt-Bi/supported catalysts is that the Bi species is incorporated in the molecular skeletal structure in Pt/Bi-MCM-41, while it is present on the support surface for the other catalysts. Thus, Figure 4 indicates a preference for Bi on the support surface. Further discussion regarding this point is provided in "mechanism of glycerol selective oxidation" section.

Two additional observations about the data in Figure 4 are noteworthy. First, the maximum DHA value for Pt-Bi/AC is similar to that reported previously,[21] while that for Pt-Bi/MCM-41 is larger. Second, for all catalysts, the DHA yield

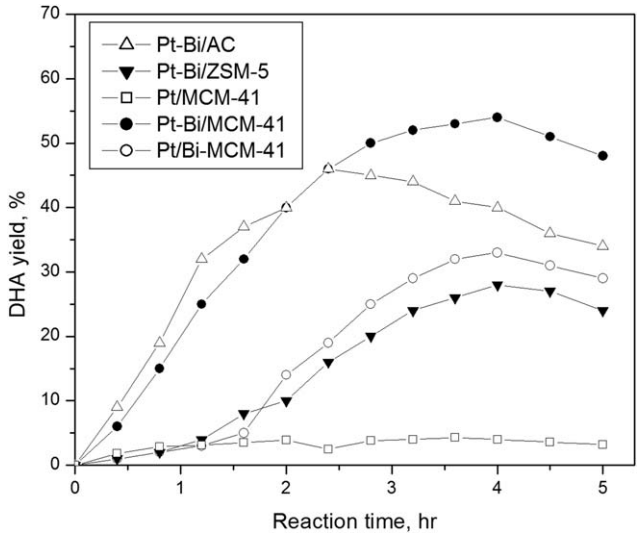


Figure 4. Kinetic behavior of different catalysts for glycerol conversion to DHA.

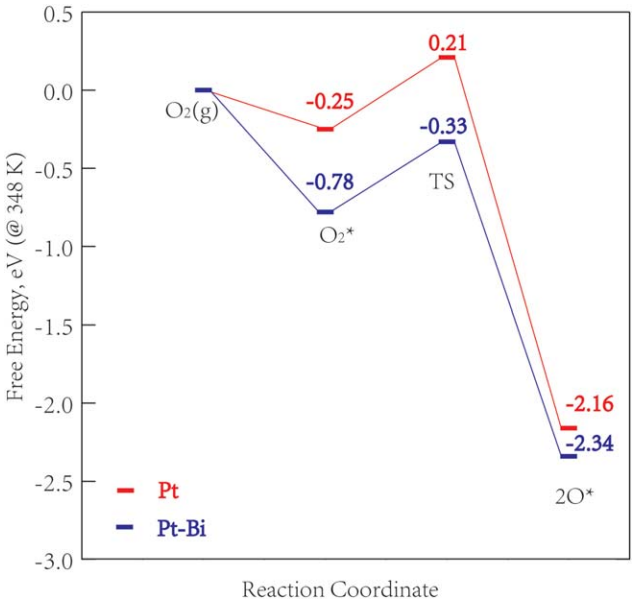


Figure 5. Energy diagram for dissociative adsorption of oxygen on Pt and Pt-Bi surfaces.

[Color figure can be viewed in the online issue, which is available at wileyonlinelibrary.com.]

reaches a maximum value at a specific time. Beyond this period, DHA degrades to other products, as discussed in detail previously.[22]

Model development for oxidized bismuth on Pt(111) surface

Based on the kinetic data for different catalysts from Figure 4, two general conclusions can be obtained, as follows. (1) Surface Bi on Pt surface is required to selectively convert glycerol by secondary –OH oxidation to product DHA, while Pt alone converts glycerol by primary –OH oxidation to GLA. (2) When MCM-41 is used as a catalyst support, high yield of DHA is achieved due to its high surface area, uniform pore structure and high Pt dispersion. Thus, to better understand these experimental results and then to obtain insight into the mechanism of glycerol conversion to DHA on the Pt-Bi catalyst, oxidized bismuth models based on DFT calculations are developed, and a catalytic cycle is proposed in the next sections, where support effects are not explicitly considered to make the theoretical models tractable.

Dissociative Adsorption of Oxygen on Pt(111) and Bi-Pt(111) Surfaces. Since the Pt-Bi catalyst is reduced using SBH (see "catalyst preparation" section) before each testing reaction, metallic Pt-Bi catalyst is obtained until O_2 enters the reactor. By DFT calculations, it is found that, thermodynamically, bismuth segregates to the Pt(111) surface (Supporting Information Figure S1) when the molar ratio of Pt : Bi is 3:1, which was consistent with the experimental XPS and XRD analysis of Kimura et al.[7] Note that DFT employed 3:1 Pt : Bi ratio is close to the experimental value used in this work. Additionally, Supporting Information Figure S2 shows that surface energies of Bi adatom models are similar to those of Bi segregation models. Thus, it is reasonable to employ Bi adatoms and a clean Pt (111) substrate to model Pt-Bi bimetallic catalysts, particularly given that operating conditions and catalyst morphology, which are not considered in our computational models, will all impact the exact coverage of Bi on the catalyst surface.

In the experiments, once O_2 (of partial pressure 30 psig, typically) enters the reactor, the metallic Pt-Bi catalyst could be oxidized, as noted above. To evaluate this effect, DFT calculations were conducted regarding O_2 dissociative adsorption on

Table 3. The TOF and DHA Selectivity Values Over Five Different Catalysts

	Pt-Bi/AC		Pt-Bi/ZSM-5		Pt/MCM-41		Pt-Bi/MCM-41		Pt/Bi-MCM-41	
Reaction time (h)	TOF (min^{-1})	DHA selectivity (%)	TOF (min^{-1})	DHA selectivity (%)	TOF (min^{-1})	DHA selectivity (%)	TOF (min^{-1})	DHA selectivity (%)	TOF (min^{-1})	DHA selectivity (%)
0.00	0.00	0.00	0.00	0.00	0.00	0.00	0.00	0.00	0.12	0.00
0.40	5.27	77.12	3.49	14.29	4.12	15.25	4.34	36.78	3.51	9.09
0.80	6.90	62.78	3.18	11.73	5.40	9.39	4.09	46.34	2.81	11.34
1.20	7.10	67.51	3.33	11.39	5.56	6.50	4.11	50.30	2.96	14.01
1.60	6.60	63.62	3.23	14.88	5.16	5.92	3.84	52.19	3.13	19.91
2.00	5.97	60.39	3.57	29.14	4.68	5.83	3.33	60.54	2.89	21.04
2.40	5.71	61.07	3.43	33.04	4.47	3.26	3.00	62.60	2.83	27.94
2.80	5.10	56.45	3.45	38.00	3.99	4.76	2.79	64.29	2.77	30.34
3.20	4.49	55.72	3.32	39.28	3.51	4.98	2.51	64.06	2.79	31.65
3.60	4.02	50.92	3.17	41.07	3.15	5.30	2.29	63.92	2.66	31.32
4.00	3.64	49.75	2.98	39.90	2.85	4.90	2.07	65.26	2.47	33.73
4.50	3.33	44.03	2.68	36.95	2.60	4.30	1.90	59.98	2.22	31.67
5.00	3.14	38.99	2.52	33.56	2.46	3.64	1.74	54.88	2.08	27.28

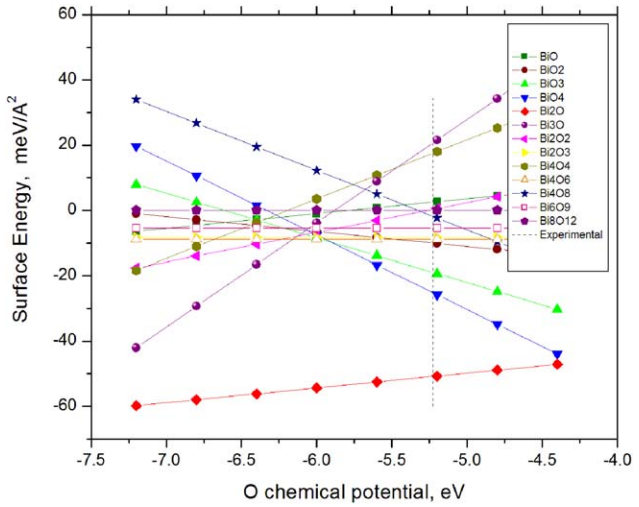


Figure 6. Phase diagram for oxidized bismuth models on Pt(111) surface.

[Color figure can be viewed in the online issue, which is available at wileyonlinelibrary.com.]

Pt and Pt-Bi surfaces, leading to oxidized bismuth catalysts. In these calculations, a 4-layer p(4 × 4) unit cell of Pt(111) was used to model the Pt catalyst, while two Bi adatoms on each such Pt slab were used to model the Pt-Bi catalyst. Initial, transition and final geometries of O_2 dissociative adsorption on these two catalysts are shown in Supporting Information Figure S3. More details and discussion are available in the next section on "phase diagrams for oxidized bismuth models on the Pt(111) surface." The energy diagram for O_2 dissociative adsorption is shown in Figure 5.

All reported barriers in Figure 5 are effective activation barriers, defined as the difference between the most stable

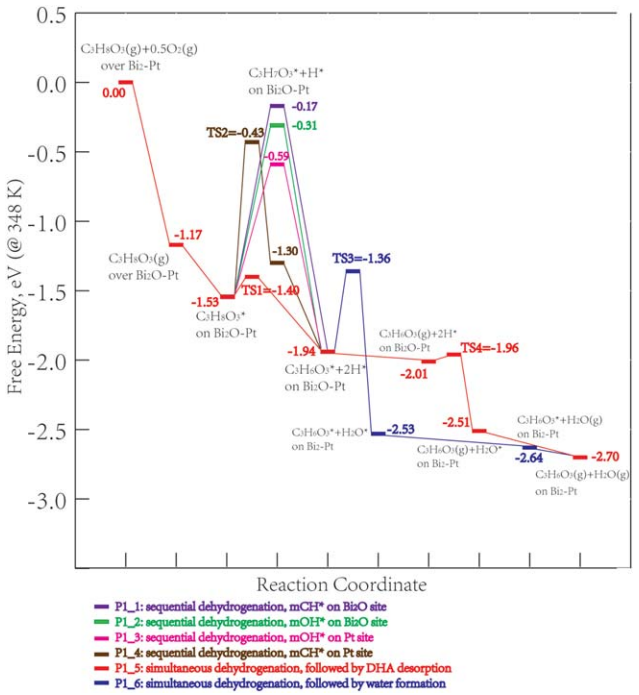


Figure 7. Energy diagram for DHA formation pathways on the Pt-Bi surface.

[Color figure can be viewed in the online issue, which is available at wileyonlinelibrary.com.]

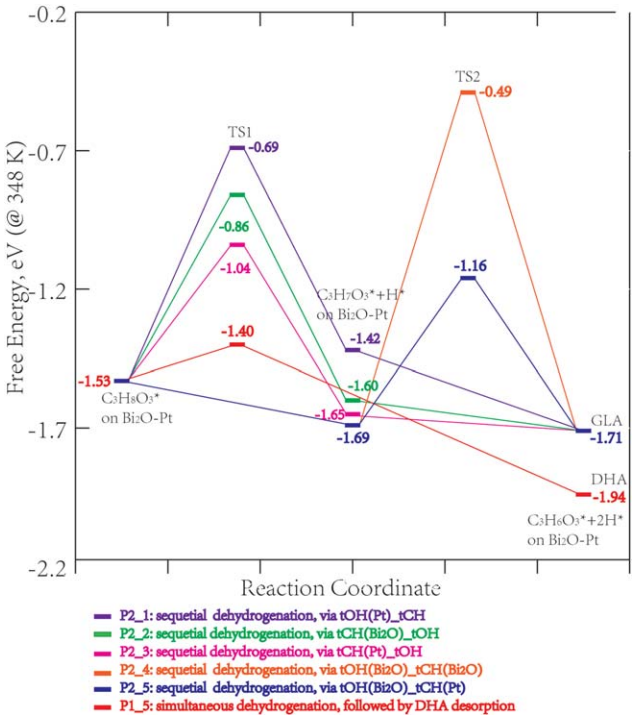


Figure 8. Energy diagram for primary vs. secondary hydroxyl oxidation of glycerol on the Pt-Bi surface.

[Color figure can be viewed in the online issue, which is available at wileyonlinelibrary.com.]

adsorption configuration of the reactant and the lowest energy transition state. The energy data reported here may be initially interpreted in terms of a basic Sabatier analysis.[64] In this model, a direct comparison between the barriers of various elementary steps is made, and the pathway with the lowest such barrier is associated with the most favored reaction mechanism. This approximate interpretation effectively assumes that surface coverages are ideal (close to unity) and that reverse reactions are not significant. The first approximation implies that reaction rates are interpreted based on rate constants, while the second approximation is motivated by the fact that surface oxygen will likely be removed very quickly by reaction with adsorbed hydrogen atoms and formation of water. Likewise, Figure 7 and 8 will be interpreted using the same strategy.

Figure 5 demonstrates that, in terms of both kinetics and thermodynamics, the Pt-Bi catalyst is easier to oxidize than the Pt catalyst, implying that oxidized bismuth may be a viable active site for glycerol selective oxidation (dehydrogenation) to DHA.

Phase Diagrams for Oxidized Bismuth Models on the Pt(111) Surface. To develop appropriate models of oxidized bismuth on the Pt(111) surface, we consider a surface in contact with an oxygen atmosphere associated with a given oxygen partial pressure and temperature, which means that the environment acts as an oxygen reservoir. As described in Eq. 3, the surface free energy is a function of the O_2 partial pressure, temperature, and the numbers of O and Bi in the Bi_xO_y cluster. A variety of Bi_xO_y clusters were evaluated using the criterion of surface energy, which are shown in Figure 6. Among these models, different nominal oxidation states of Bi (+8, +6, +4, +3, +2, and +1), different numbers of Bi and

O atoms were investigated. As discussed above, only small clusters of Bi_xO_y were focused on in this work, while selected larger clusters (e.g., Bi_8O_{12} and Bi_6O_9) were mentioned for comparison. Note that not all of the optimized clusters in Figure 6 are truly stable (see also Figure S4). For example, BiO, BiO_2, BiO_3 models spontaneously dissociate into isolated Bi atoms and O atoms, while Bi_2O_2 dissociates into a Bi_2O cluster and an isolated O atom. Figure 6 shows that the Bi_2O cluster is the most favorable under the experimental operating conditions (dashed line, $\mu_O = -5.23$ eV). As a result, the Bi_2O-Pt(111) model is used to analyze the mechanism of glycerol selective oxidation in the next sections.

Mechanism of glycerol selective oxidation

In this section, we first analyze DHA formation, and then consider selective dehydrogenation (oxidation) of primary vs. secondary hydroxyl groups in glycerol.

DHA Formation Pathways on Pt-Bi Surface (Pathway P1). After O_2 dissociative adsorption and the Bi_2O cluster formation, glycerol is adsorbed on the Bi_2O-Pt(111) surface. Compared to the surfaces of metallic Pt(111) and Bi-Pt(111), it is found that the BE of glycerol on Bi_2O-Pt(111) surface becomes more negative by ~0.4 eV (see Table S2), which means oxidized bismuth stabilizes glycerol.

To form DHA, typically, after glycerol is adsorbed, it is considered to undergo two sequential elementary steps in one of two different sequences: dehydrogenation on the middle C atom followed by dehydrogenation on the middle O atom or dehydrogenation on the middle O atom followed by dehydrogenation on the middle C atom. In addition, it is found these two steps could occur simultaneously at the interface of Pt and Bi_2O, while sequential dehydrogenation occurs either at Pt site or Bi_2O site. Dehydrogenation steps are followed by water formation and desorption of DHA and water. Thus, based on considering different dehydrogenation steps and desorption steps, the following six pathways were evaluated and listed in Figure 7. In the following, for convenience, we will denote mOH* and mCH* representing dehydrogenation on secondary hydroxyl and middle carbon atoms in glycerol, respectively.

- P1_1: sequential dehydrogenation, mCH* on Bi_2O site;
- P1_2: sequential dehydrogenation, mOH* on Bi_2O site;
- P1_3: sequential dehydrogenation, mOH* on Pt site;
- P1_4: sequential dehydrogenation, mCH* on Pt site;
- P1_5: simultaneous dehydrogenation, followed by DHA desorption;
- P1_6: simultaneous dehydrogenation, followed by water formation.

For each case in Figure 7, the energy zero corresponds to gas phase glycerol and the appropriate clean surface. It is assumed that all the pathways in Figure 7 start with two steps: oxygen dissociative adsorption (metallic catalyst converted to oxide catalyst) and glycerol adsorption, both of which have been discussed in previous sections. Via P1_5, a simultaneous dehydrogenation step shows lowest energy barrier (0.13 eV), in which H atom from secondary hydroxyl moves to Bi_2O site, while H atom from middle carbon atom moves to the surface of Pt(111) (see Supporting Information Figure S5), forming DHA. It indicates a cooperative effect, between platinum species as the primary component and bismuth species as the promoter, on DHA formation from glycerol. There are two possibilities following the simultaneous dehydrogenation: DHA desorption followed by H_2O formation and desorption (P1_5), and water formation followed by DHA and water desorption (P1_6). As shown in Figure 7, P1_5 is more favorable than P1_6, because water formation requires an energy barrier of 0.58 eV in the presence of binding DHA in P1_6, while it requires only 0.05 eV in P1_5 after DHA desorbs. Note that in both P1_5 and P1_6, after DHA and H_2O desorb in the last step, metallic Bi_2-Pt(111) catalyst is regenerated, forming the same state in which it started.

Another pathway, directly starting from binding glycerol (−1.53 eV) to form binding DHA and H_2O (−2.53 eV), without dehydrogenated intermediates and surface diffusion of H atoms, was also considered. Although this seems thermodynamically favorable, it was excluded because a metastable intermediate (−1.94 eV) and two transition states (TS1 = −1.40 eV and TS3 = −1.36 eV) were found, which includes a higher reaction barrier of 0.58 eV (from −1.94 eV to −1.36 eV) than its competing step (from −1.94 eV to −2.01 eV and then −1.96 eV). Moreover, other possibilities of water formation mechanisms were tested, but it turns out H_2O formation at bismuth site is more favorable than at Pt sites (Supporting Information Figure S6). Therefore, only bismuth was considered for H_2O formation site.

For sequential dehydrogenation pathways (P1_1, P1_2, and P1_3) in Figure 7, the energies (−0.17, −0.31, and −0.59 eV) of these intermediates are even higher than the transition state (TS1= −1.40 eV) of P1_5. Therefore, P1_1, P1_2, and P1_3 are not favorable as compared with P1_5, although transition states of these pathways were not located since their energies should be even higher than intermediate energies. For P1_4, although the energy of its dehydrogenated intermediate is low (−1.30 eV), the energy of the transition state (TS2 = −0.43 eV) is still higher than the transition state (TS1 = −1.40 eV) of P1_5. As a result, all the sequential dehydrogenation pathways, either at the Pt site or the Bi_2O site, are not favorable as compared to the simultaneous dehydrogenation pathway P1_5. Thus, P1_5 is considered to be the most favored reaction mechanism.

Primary vs. Secondary Selective Dehydrogenation of Glycerol on Pt-Bi Surface (Pathway P2). In the "DHA formation pathways on Pt-Bi surface" section (P1), only secondary selective dehydrogenation of glycerol was considered. The comparison of secondary vs. primary dehydrogenation is discussed in the current section.

Oxidation of the secondary hydroxyl group is a competing reaction of the primary hydroxyl group oxidation. Since three main products, DHA, glyceraldehyde (GLA), and glyceric acid, were found experimentally, and glyceric acid is easily obtained from further oxidation of GLA, only DHA and GLA were considered as oxidative products in the DFT calculations. In our prior work,[22] it was shown that there was no isomerization between DHA and GLA. Thus, only two reactions (GLY to DHA and GLY to GLA) are investigated below. As noted above, all the pathways start with two steps: oxygen dissociative adsorption (metallic catalyst converted to oxide catalyst) and glycerol adsorption. The same assumption is used for the primary vs. secondary hydroxyl selective dehydrogenation comparison. In addition, for simplicity, desorption of products is not explicitly calculated in this pathway, and only dehydrogenation steps are investigated.

To form GLA, glycerol needs to undergo two other elementary steps in one of two different sequences: dehydrogenation on the terminal C atom followed by dehydrogenation on the terminal O atom (labeled as tCH_tOH), or dehydrogenation on the terminal O atom followed by dehydrogenation on the

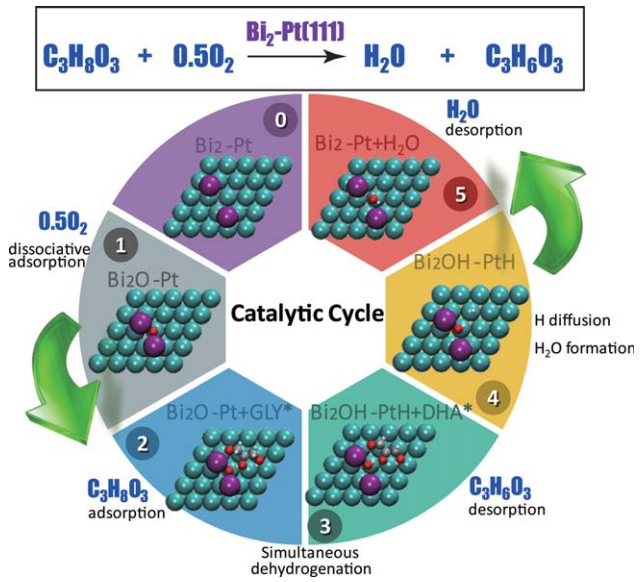


Figure 9. Proposed catalytic cycle of Pt-Bi for DHA ($C_3H_6O_3$) formation from glycerol ($C_3H_8O_3$).

[Color figure can be viewed in the online issue, which is available at wileyonlinelibrary.com.]

terminal C atom (labeled as tOH_tCH). Thus, pathways P2_1–P2_5 are shown in Figure 8. The P1_5 in Figure 7 is also shown in Figure 8, as a reference for primary dehydrogenation pathways.

No simultaneous dehydrogenation pathways are found for the primary dehydrogenation of glycerol, forming glyceraldehyde (GLA). Similar to the case for DHA formation from glycerol dehydrogenation, both the Bi_2O site and the Pt site were considered. For the first dehydrogenation steps, P2_1 (tOH on Pt site), P2_2 (tCH on Bi_2O site), and P2_3 (tCH on Pt site) have higher energy barriers (−0.69, −0.86, and −1.04 eV) than transition state (TS1 = −1.40 eV) of P1_5. This means they are unfavorable in the first dehydrogenation step. Thus, no further calculation for the second dehydrogenation was conducted. It is, however, very favorable when dehydrogenation occurs on the primary hydroxyl at Bi_2O site (P2_4 and P2_5), since it is found than such a step has no transition state and energy barrier, and is thus controlled by thermodynamics. Further calculations were conducted for secondary dehydrogenation steps. P2_4 corresponds to dehydrogenation from the terminal carbon atom at the Bi_2O site, while P2_5 refers to the same process at the Pt site. It turns out that both P2_4 and P2_5 have higher energies of transition states (TS2 = −0.49 and −1.16 eV) than the transition state (TS1 = −1.40 eV) of P1_5. It is thus deduced from Figure 8 that DHA, as a secondary hydroxyl oxidation product, is more favorable on Pt-Bi bimetallic catalyst than GLA, the primary hydroxyl oxidation product, which is consistent with the experimental results in the current work and other published results,[7,21,65]

As noted in the experiment part, ratios of Pt and Bi atoms on the surface are ∼2:1–3:1, corresponding to the ratio of ∼4:1–6:1 between Pt and Bi_2O sites. Using Arrhenius equation ($k = A_0*\exp(-Ea/k_B/T)$) and T = 348 K, E_a decrease by ∼0.3 eV of Bi_2O site (as compared to Pt site), results in the increase of reaction rate constant by $\sim 10^4$ times, which is much more notable than site number effect. Thus, the site numbers of Bi_2O and Pt do not play an important role for tuning reaction rates.

Proposed catalytic cycle of glycerol selective oxidation to DHA at Pt-Bi bimetallic surface

Based on the above discussion, a proposed catalytic cycle of glycerol secondary hydroxyl group oxidation on Pt-Bi bimetallic catalyst is illustrated in Figure 9. The cycle starts with a metallic catalyst (Bi_2-Pt), followed by oxygen dissociative adsorption on bismuth site (Bi_2O-Pt), glycerol binding in the interface of Bi_2O and Pt (Bi_2O-Pt + GLY*), simultaneous dehydrogenation (Bi_2OH + PtH + DHA*), DHA desorption (Bi_2OH + PtH), and ends with H_2O formation and desorption (Bi_2-Pt).

Concluding Remarks

In the present work, the performance of five different catalysts (Pt-Bi/AC, Pt-Bi/ZSM-5, Pt/MCM-41, Pt-Bi/MCM-41, and Pt/Bi-MCM-41) was investigated in terms of glycerol selective oxidation to DHA. The experimental kinetic behaviors show that a bimetallic Pt-Bi catalyst loaded on the ordered mesoporous support MCM-41 exhibits the highest DHA yield. Using a periodic slab-model density-functional approach, an oxidized bismuth on Pt(111) model was selected and developed to represent this bimetallic Pt-Bi catalyst. Based on the calculation results, a favorable pathway and catalytic cycle of DHA formation were proposed. Both experimental and computational results indicate that Bi segregation to the surface is relevant to the formation of active sites, which require Bi and Pt in close proximity to enable cooperative effects for selective DHA formation from glycerol.

Acknowledgments

This work was supported by the R. Games Slayter Fund (A. Varma) and by the Designing Materials to Revolutionize and Engineer our Future (DMREF award #CBET1437219) program of the National Science Foundation (J. Greeley). Computational resources provided through the National Energy Research Scientific Computing Center are also acknowledged. The authors also thank Ms. Paulami Majumdar for helpful discussions.

Notation

A = area of a given surface, $Å^2$
A_0 = pre-exponential factor, s^{-1}
BE = binding energy of an adsorbate, eV
E_a = energy barrier of a given reaction, eV
E_{ad} = energy of a gas molecular adsorbate, eV
$E_{ad/slab}$ = energy of a binding adsorbate and a clean slab, eV
E_{IS} = energy of an initial state, eV
E_{slab} = energy of a clean slab, eV
E_{TS} = energy of a transition state, eV
G = Gibbs free energy, eV
$g^{bulk}_{Bi_2O_3}$ = Gibbs free energy of Bi_2O_3 bulk, eV
g^{bulk}_{Bi} = Gibbs free energy of Bi bulk, eV
k = reaction rate constant, s^{-1}
k_B = Boltzmann constant, J/K
p = pressure, Pa
T = temperature, K
x = number of Bi atoms in a Bi_xO_y cluster
y = number of O atoms in a Bi_xO_y cluster
μ_{Bi} = bismuth chemical potential, eV
μ_O = oxygen chemical potential, eV
$\gamma(T,p)$ = surface free energy, eV

Literature Cited

1. Aransiola EF, Ojumu TV, Oyekola OO, Madzimbamuto TF, Ikhu-Omoregbe DIO. A review of current technology for biodiesel production: state of the art. *Biomass Bioenerg*. 2014;61:276–297.

2. Liu Y, Yan YJ, Hu F, Yao AN, Wang ZC, Wei FX. Transesterification for biodiesel production catalyzed by combined lipases: optimization and kinetics. *Aiche J*. 2010;56:1659–1665.
3. Ayoub M, Abdullah AZ. Critical review on the current scenario and significance of crude glycerol resulting from biodiesel industry towards more sustainable renewable energy industry. *Renew Sust Energ Rev*. 2012;16:2671–2686.
4. Yang FX, Hanna MA, Sun RC. Value-added uses for crude glycerol-a byproduct of biodiesel production. *Biotech. Biofuels* 2012;5:13.
5. Mallat T, Bodnar Z, Hug P, Baiker A. Selective oxidation of cinnamyl alcohol to cinnamaldehyde with air over Bi-Pt/alumina catalysts. *J Catal*. 1995;153:131–143.
6. Liang D, Gao J, Wang JH, Chen P, Hou ZY, Zheng XM. Selective oxidation of glycerol in a base-free aqueous solution over different sized Pt catalysts. *Catal Commun*. 2009;10:1586–1590.
7. Kimura H, Tsuto K, Wakisaka T, Kazumi Y, Inaya Y. Selective oxidation of glycerol on a platinum bismuth catalyst. *Appl Catal A-Gen*. 1993;96:217–228.
8. Kimura H. Selective oxidation of glycerol on a Platinum-bismuth catalyst by using a Fixed-bed reactor. *Appl Catal A-Gen*. 1993;105:147–158.
9. Norskov JK, Scheffler M, Toulhoat H. Density functional theory in surface science and heterogeneous catalysis. *Mrs Bull*. 2006;31:669–674.
10. Lee JC, Xu Y, Huber GW. High-throughput screening of monometallic catalysts for aqueous-phase hydrogenation of biomass-derived oxygenates. *Appl Catal B-Environ*. 2013;140:98–107.
11. Kapur N, Shan B, Hyun J, Wang LG, Yang S, Nicholas JB, Cho K. First-principles study of CO oxidation on bismuth-promoted pt(111) surfaces. *Mol Simulat*. 2011;37:648–658.
12. Jang YH, Goddard WA. Selective oxidation and ammoxidation of propene on bismuth molybdates, ab initio calculations. *Top Catal*. 2001;15:273–289.
13. Hanna TA. The role of bismuth in the SOHIO process. *Coordin Chem Rev*. 2004;248:429–440.
14. Meusinger J, Corma A. Activation of hydrogen on Zeolites - kinetics and mechanism of N-heptane cracking on H-Zsm-5 zeolites under high hydrogen pressure. *J Catal*. 1995;152:189–197.
15. Valle B, Alonso A, Atutxa A, Gayubo AG, Bilbao J. Effect of nickel incorporation on the acidity and stability of HZSM-5 zeolite in the MTO process. *Catal Today*. 2005;106:118–122.
16. Kim YT, Jung KD, Park ED. Gas-phase dehydration of glycerol over ZSM-5 catalysts. *Micropor Mesopor Mat*. 2010;131:28–36.
17. Kresge CT, Leonowicz ME, Roth WJ, Vartuli JC, Beck JS. Ordered mesoporous Molecular-sieves synthesized by a Liquid-crystal template mechanism. *Nature*. 1992;359:710–712.
18. Chen Y, Wu YL, Ding RR, Zhang P, Liu J, Yang MD, Zhang P. Catalytic hydrothermal liquefaction of D. tertiolecta for the production of Bio-oil over different acid/base catalysts. *AIChE J*. 2015;61:1118–1128.
19. Carvalho WA, Varaldo PB, Wallau M, Schuchardt U. Mesoporous redox molecular sieves analogous to MCM-41. *Zeolites*. 1997;18:408–416.
20. Chen S, Meng YL, Zhao YJ, Ma XB, Gong JL. Selective oxidation of methanol to dimethoxymethane over mesoporous Al-P-V-O catalysts. *AIChE J*. 2013;59:2587–2593.
21. Hu WB, Knight D, Lowry B, Varma A. Selective oxidation of glycerol to dihydroxyacetone over Pt-bi/C catalyst: optimization of catalyst and reaction conditions. *Ind Eng Chem Res*. 2010;49:10876–10882.
22. Hu WB, Lowry B, Varma A. Kinetic study of glycerol oxidation network over Pt-Bi/C catalyst. *Appl Catal B-Environ*. 2011;106:123–132.
23. Liu B, Greeley J. A density functional theory analysis of trends in glycerol decomposition on close-packed transition metal surfaces. *Phys Chem Chem Phys*. 2013;15:6475–6485.
24. Liu B, Greeley J. Density functional theory study of selectivity considerations for C-C versus C-O bond scission in glycerol decomposition on Pt(111). *Top Catal*. 2012;55:280–289.
25. Liu B, Greeley J. Decomposition pathways of glycerol via C-H, O-H, and C-C bond scission on pt(111): a density functional theory study. *J Phys Chem C*. 2011;115:19702–19709.
26. Chen CY, Li HX, Davis ME. Studies on mesoporous materials.1. Synthesis and characterization of Mcm-41. *Microporous Mater*. 1993;2:17–26.
27. Corma A, Navarro MT, Pariente JP. Synthesis of an ultralarge pore titanium silicate isomorphous to MCM-41 and its application as a catalyst for selective oxidation of hydrocarbons. *J Chem Soc Chem Comm*. 1994;147–148.
28. Benson JE, Boudart M. Hydrogen-oxygen titration method for the measurement of supported platinum surface areas. *J Catal*. 1965;4:704–710.
29. Kresse G, Furthmuller J. Efficiency of ab-initio total energy calculations for metals and semiconductors using a plane-wave basis set. *Comp Mater Sci*. 1996;6:15–50.
30. Kresse G, Hafner J. Ab-initio Molecular-dynamics simulation of the Liquid-metal Amorphous-semiconductor transition in germanium. *Phys Rev B*. 1994;49:14251–14269.
31. Kresse G, Joubert D. From ultrasoft pseudopotentials to the projector augmented-wave method. *Phys Rev B*. 1999;59:1758–1775.
32. Blochl PE. Projector Augmented-wave method. *Phys Rev B*. 1994; 50:17953–17979.
33. Perdew JP, Chevary JA, Vosko SH, Jackson KA, Pederson MR, Singh DJ, Fiolhais C. Atoms, molecules, solids, and Surfaces - applications of the generalized gradient approximation for exchange and correlation. *Phys Rev B*. 1992;46:6671–6687.
34. Methfessel M, Paxton AT. High-precision sampling for Brillouin-zone integration in metals. *Phys Rev B*. 1989;40:3616–3621.
35. Monkhorst HJ, Pack JD. Special points for Brillouin-zone integrations. *Phys Rev B*. 1976;13:5188–5192.
36. Kittel C. *Introduction to Solid State Physics*, *8th ed*. New York: Wiley, 2005.
37. Zhao ZJ, Moskaleva LV, Aleksandrov HA, Basaran D, Rosch N. Ethylidyne formation from ethylene over Pt(111): a mechanistic study from First-principle calculations. *J Phys Chem C*. 2010;114:12190–12201.
38. Alcala R, Mavrikakis M, Dumesic JA. DFT studies for cleavage of C-C and C-O bonds in surface species derived from ethanol on Pt(111). *J Catal*. 2003;218:178–190.
39. Zhao ZJ, Greeley JP. Identification of surface intermediates during ethylidyne formation on Pt(111) by calculation of infrared intensities and deuterium isotope shifts. *Surf Sci*. 2015;640:112–118.
40. Henkelman G, Jonsson H. A dimer method for finding saddle points on high dimensional potential surfaces using only first derivatives. *J Chem Phys*. 1999;111:7010–7022.
41. Mills G, Jonsson H, Schenter GK. Reversible work Transition-state Theory - application to dissociative adsorption of hydrogen. *Surf Sci*. 1995;324:305–337.
42. Henkelman G, Jonsson H. Improved tangent estimate in the nudged elastic band method for finding minimum energy paths and saddle points. *J Chem Phys*. 2000;113:9978–9985.
43. Gokhale AA, Kandoi S, Greeley JP, Mavrikakis M, Dumesic JA. Molecular-level descriptions of surface chemistry in kinetic models using density functional theory. *Chem Eng Sci*. 2004;59:4679–4691.
44. Chang CR, Zhao ZJ, Kohler K, Genest A, Li J, Rosch N. Theoretical study on the leaching of palladium in a CO atmosphere. *Catal Sci Technol*. 2012;2:2238–2248.
45. Eberhart R, Kennedy J. *A new optimizer using particle swarm theory*. In: *IEEE*, New York, NY, 1995:39–43.
46. Wang YC, Lv JA, Zhu L, Ma YM. Crystal structure prediction via particle-swarm optimization. *Phys Rev B*. 2010;82:094116.
47. Lu SH, Wang YC, Liu HY, Miao MS, Ma YM. Self-assembled ultrathin nanotubes on diamond (100) surface. *Nat Commun*. 2014;5:3666.
48. Reuter K, Scheffler M. Composition, structure, and stability of RuO2(110) as a function of oxygen pressure. *Phys Rev B*. 2002;65: 035406.
49. Reuter K, Scheffler M. First-principles atomistic thermodynamics for oxidation catalysis: surface phase diagrams and catalytically interesting regions. *Phys Rev Lett*. 2003;90:046103.
50. Brunauer S, Emmett PH, Teller E. Adsorption of gases in multimolecular layers. *J Am Chem Soc*. 1938;60:309–319.
51. Serrano-Ruiz JC, Dumesic JA. Catalytic routes for the conversion of biomass into liquid hydrocarbon transportation fuels. *Energ Environ Sci*. 2011;4:83–99.
52. Olson DH, Kokotailo GT, Lawton SL, Meier WM. Crystal-structure and Structure-related properties of Zsm-5. *J Phys Chem-Us*. 1981; 85:2238–2243.
53. Huang LM, Guo WP, Deng P, Xue ZY, Li Q. Z. Investigation of synthesizing MCM-41/ZSM-5 composites. *J Phys Chem B*. 2000; 104:2817–2823.
54. Brunauer S, Deming LS, Deming WE, Teller E. On a theory of the van der Waals adsorption of gases. *J Am Chem Soc*. 1940;62:1723–1732.
55. Sarkisov L, Monson PA. Modeling of adsorption and desorption in pores of simple geometry using molecular dynamics. *Langmuir*. 2001;17:7600–7604.
56. Ertl G, Knözinger H, Schüth F, Weitkamp J. *Handbook of Heterogenous Catalysis*. New York: Wiley, 2008.
57. Corey EJ, Gilman NW, Ganem BE. New methods for the oxidation of aldehydes to carboxylic acids and esters. *J Am Chem Soc*. 1968; 90:5616–5617.
58. Carrettin S, McMorn P, Johnston P, Griffin K, Hutchings GJ. Selective oxidation of glycerol to glyceric acid using a gold catalyst in aqueous sodium hydroxide. *Chem Commun*. 2002;696–697.

59. Carrettin S, McMorn P, Johnston P, Griffin K, Kiely CJ, Hutchings GJ. Oxidation of glycerol using supported Pt, Pd and Au catalysts. *Phys Chem Chem Phys*. 2003;5:1329–1336.
60. Zhao XS, Lu GQM, Millar GJ. Advances in mesoporous molecular sieve MCM-41. *Ind Eng Chem Res*. 1996;35:2075–2090.
61. Choi JS, Kim DJ, Chang SH, Ahn WS. Catalytic applications of MCM-41 with different pore sizes in selected liquid phase reactions. *Appl Catal A-Gen*. 2003;254:225–237.
62. Corma A, Martinez A, Martinezsoria V, Monton JB. Hydrocracking of vacuum Gas-oil on the novel mesoporous MCM-41 aluminosilicate catalyst. *J Catal*. 1995;153:25–31.
63. Qian G, Ji D, Lu GM, Zhao R, Qi YX, Suo JS. Bismuth-containing MCM-41: synthesis, characterization, and catalytic behavior in liquid-phase oxidation of cyclohexane. *J Catal*. 2005;232:378–385.
64. Bligaard T, Norskov JK, Dahl S, Matthiesen J, Christensen CH, Sehested J. The Bronsted-Evans-polanyi relation and the volcano curve in heterogeneous catalysis. *J Catal*. 2004;224:206–217.
65. Worz N, Brandner A, Claus P. Platinum-Bismuth-catalyzed oxidation of glycerol: kinetics and the origin of selective deactivation. *J Phys Chem C*. 2010;114:1164–1172.

Manuscript received Nov. 24, 2015, and revision received June 18, 2016.

An Experimental and Theoretical Study of Glycerol Oxidation to 1,3-Dihydroxyacetone over Bimetallic Pt-Bi Catalysts

Yang Xiao[1], Zhi-Jian Zhao[1, 2], Jeffrey Greeley[1], Guomin Xiao[3] and Arvind Varma[1*]

1. School of Chemical Engineering, Purdue University, West Lafayette, IN 47907-2100, USA.

2. Key Laboratory for Green Chemical Technology of Ministry of Education, School of Chemical Engineering and Technology, Tianjin University, Collaborative Innovation Center of Chemical Science and Engineering, Tianjin 300072, PRC.

3. School of Chemistry and Chemical Engineering, Southeast University, Nanjing 211189, PRC.

*To whom correspondence should be addressed. Telephone: +1-(765) 494-4075. Fax: +1-(765) 494-0805. E-mail: avarma@purdue.edu.

SUPPLEMENTARY INFORMATION

Surface energy calculations for Pt-Bi slabs

Correlation of surface energy and oxygen chemical potential

Table Captions

Table S1. Profiles of concentrations over five different catalysts

Table S2. Binding energies of glycerol on different sites and models

*To whom correspondence should be addressed. Telephone: +1-(765) 494-4075. Fax: +1-(765) 494-0805. E-mail: avarma@purdue.edu.

Figure Captions

Figure S1. Bi segregation on Pt(111) surface

Figure S2. Bi adatom models on Pt(111) surface

Figure S3. Initial, transition and final geometries of O_2 dissociative adsorption on Pt and Pt-Bi models

Figure S4. Geometries of different oxidized bismuth models

Figure S5. Initial, transition and final geometries of glycerol selective oxidation to DHA on Bi_2O_Pt(111) model.

Figure S6. Bismuth site vs. Platinum site for H_2O formation

Surface energy calculations for Pt-Bi slabs

We consider a series of six-layer Pt-Bi slabs. Each slab has two symmetric surfaces and is considered to be cleaved from Pt and Bi bulks. The surface energies for these slabs are defined as:

$$\gamma = \frac{1}{2A}\left[E^{slab}(Bi,Pt) - n_{Pt}E_{Pt}^{bulk} - n_{Bi}E_{Bi}^{bulk}\right] \quad \text{(S-1)}$$

Eq. (1) is used in Figure S1 and S2.

Correlation of surface energy and oxygen chemical potential

We consider a surface in contact with an oxygen atmosphere described by an oxygen pressure, p, and temperature, T. This means that the environment acts as a reservoir, because it can give (or take) any amount of oxygen to (or from) the sample without changing the temperature or pressure. The appropriate thermodynamic potential required to describe such a system is the
Gibbs free energy, G(T, p, x, y), which depends also on the number of Bi and O atoms in each model. The most stable surface composition and geometry is then the one that minimizes the surface free energy, defined as:

$$\gamma(T,p) = \frac{1}{A}\left[G^{slab}\left(Bi_xO_y,Pt\right) - G^{slab}(Pt) - x\mu_{Bi} - y\mu_O\right] \quad \text{(S-2)}$$

In eq. (S-2) the chemical potentials of O and Bi enter in a symmetric way. However, if there is enough bulk material, so that it acts as a thermodynamic reservoir, the potentials are in fact no longer independent, but are related by the Gibbs free energy of the bulk oxide: Bi_2O_3.

$$2\mu_{Bi} + 3\mu_O = g_{Bi_2O_3}^{bulk} \quad \text{(S-3)}$$

Thus, eq. (S-3) is derived by combining eq. (S-1) and (S-2).

$$\gamma(T,p) = \frac{1}{A}\left[G^{slab}\left(Bi_xO_y,Pt\right) - G^{slab}(Pt) - \frac{x}{2}g_{Bi_2O_3}^{bulk} + \left(\frac{3}{2}x - y\right)\mu_O\right] \quad \text{(S-4)}$$

To determine the range of allowed O chemical potentials, we used an approach described in theliterature[1].

$$min[\mu_O(T,p)] = \frac{1}{3}\left[g^{bulk}_{Bi_2O_3}(0,0) - 2g^{bulk}_{Bi}(0,0)\right] \quad \text{(S-5)}$$

$$max[\mu_O(T,p)] = \frac{1}{2}E^{total}_{O_2} \quad \text{(S-6),}$$

where structures for Bi and Bi_2O_3 bulks are from Crystallography Open Database[2] and O_2 chemical potential is from DFT calculation, $\frac{1}{2}E^{total}_{O_2}$=-4.91 eV.

Thus, the range of O chemical potentials is -7.17 eV to -4.91 eV.

Table S1. Profiles of concentrations over five different catalysts

Reaction time, h	Concentrations , mol/L			
	Glycerol	DHA	Glyceric acid	Glyceraldehyde (GLA)
Pt-Bi/AC				
0.00	1.00	0.00	0.00	0.00
0.40	0.88	0.09	0.01	0.00
0.80	0.69	0.19	0.05	0.03
1.20	0.52	0.32	0.06	0.03
1.60	0.41	0.38	0.07	0.04
2.00	0.33	0.40	0.11	0.06
2.40	0.23	0.47	0.12	0.06
2.80	0.20	0.45	0.11	0.06
3.20	0.20	0.45	0.10	0.07
3.60	0.19	0.41	0.09	0.07
4.00	0.18	0.41	0.08	0.07
4.50	0.16	0.37	0.07	0.06
5.00	0.12	0.34	0.10	0.05
Pt-Bi/ZSM-5				
0.00	1.00	0.00	0.00	0.00
0.40	0.90	0.01	0.01	0.00
0.80	0.82	0.02	0.01	0.00
1.20	0.72	0.03	0.01	0.01
1.60	0.64	0.05	0.02	0.01
2.00	0.50	0.15	0.04	0.02
2.40	0.42	0.19	0.06	0.03
2.80	0.32	0.26	0.08	0.03
3.20	0.25	0.29	0.09	0.04
3.60	0.20	0.33	0.10	0.05

4.00	0.16	0.33	0.10	0.05
4.50	0.15	0.31	0.08	0.05
5.00	0.12	0.30	0.07	0.04
		Pt/MCM-41		
0.00	1.00	0.00	0.00	0.00
0.40	0.88	0.02	0.04	0.01
0.80	0.69	0.03	0.05	0.02
1.20	0.52	0.03	0.07	0.03
1.60	0.41	0.04	0.09	0.02
2.00	0.33	0.04	0.13	0.07
2.40	0.23	0.03	0.20	0.08
2.80	0.20	0.04	0.23	0.10
3.20	0.20	0.04	0.30	0.15
3.60	0.19	0.04	0.32	0.16
4.00	0.18	0.04	0.34	0.17
4.50	0.16	0.04	0.39	0.20
5.00	0.12	0.03	0.41	0.20
		Pt-Bi/MCM-41		
0.00	1.00	0.00	0.00	0.00
0.40	0.83	0.06	0.01	0.00
0.80	0.67	0.15	0.01	0.00
1.20	0.51	0.25	0.02	0.01
1.60	0.38	0.32	0.03	0.01
2.00	0.33	0.41	0.04	0.01
2.40	0.28	0.45	0.04	0.01
2.80	0.22	0.50	0.05	0.01
3.20	0.19	0.52	0.05	0.01
3.60	0.17	0.53	0.06	0.01
4.00	0.17	0.54	0.07	0.01
4.50	0.14	0.51	0.07	0.01
5.00	0.13	0.48	0.07	0.01

Pt/Bi-MCM-41				
0.00	1.00	0.00	0.00	0.00
0.40	0.88	0.01	0.02	0.02
0.80	0.81	0.02	0.04	0.02
1.20	0.69	0.04	0.06	0.03
1.60	0.57	0.09	0.06	0.03
2.00	0.50	0.11	0.07	0.04
2.40	0.41	0.16	0.08	0.05
2.80	0.33	0.20	0.08	0.05
3.20	0.23	0.24	0.10	0.07
3.60	0.17	0.26	0.11	0.07
4.00	0.15	0.29	0.13	0.08
4.50	0.14	0.27	0.14	0.09
5.00	0.10	0.25	0.15	0.09

Table S2. Binding energies of glycerol on different sites and models

Sites & Models	BE (eV)
Pt	-0.48
PtO	-0.50
Bi-Pt	-0.53
Bi_2O-Pt	-0.93

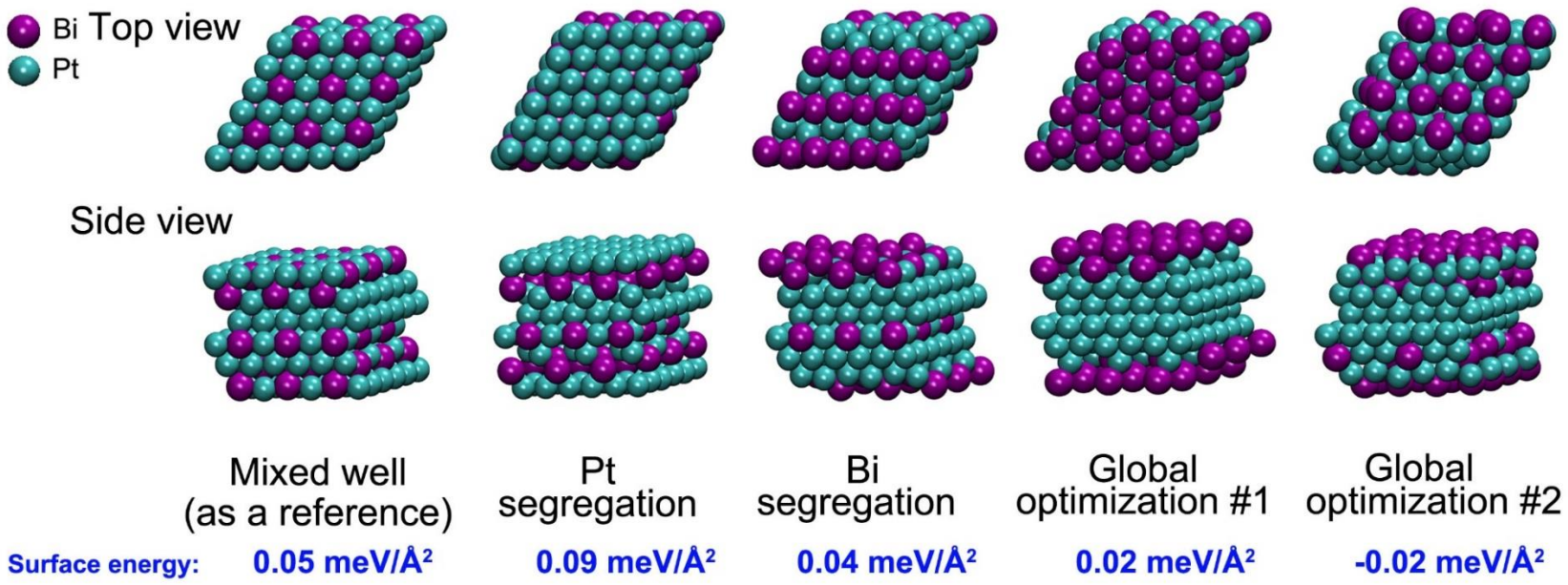


Figure S1. Bi segregation on Pt(111) surface

Model of mixed well: ratio=3, three Pt atoms and one Bi atom per layer, as a reference

Model of Pt segregation: ratio=3, exchange Bi in 1st layer with Pt in 2nd layer, energy unfavorable

Model of (simple) Bi segregation: ratio=3, exchange Pt in 1st layer with Bi in 2nd layer

Model of global opt #1 (by genetic algorithm): ratio=3, energy favorable

Model of global opt #2 (by particle swarm optimization): ratio=2.4, energy favorable

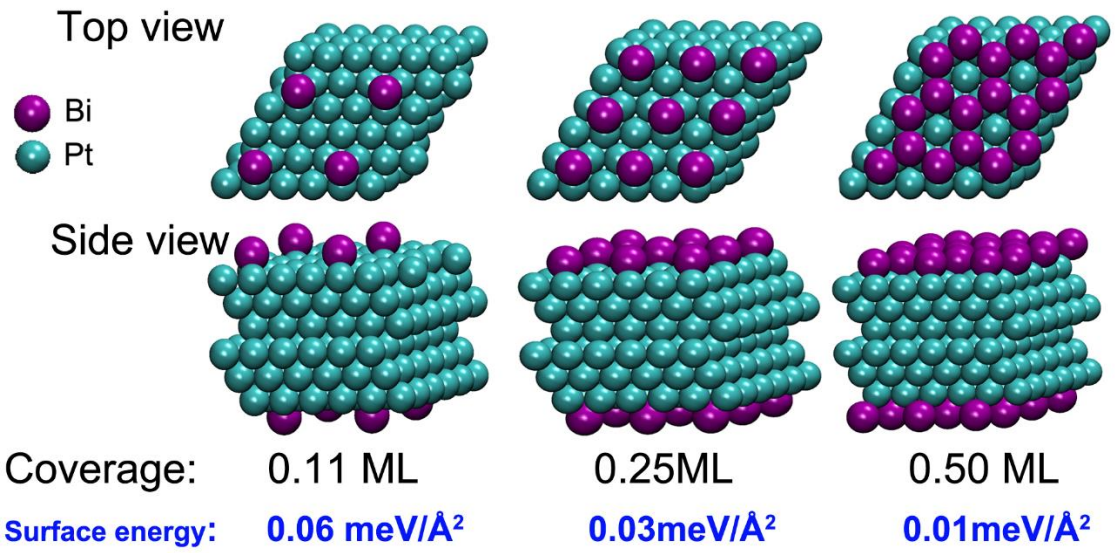


Figure S2. Bi adatom models on Pt(111) surface

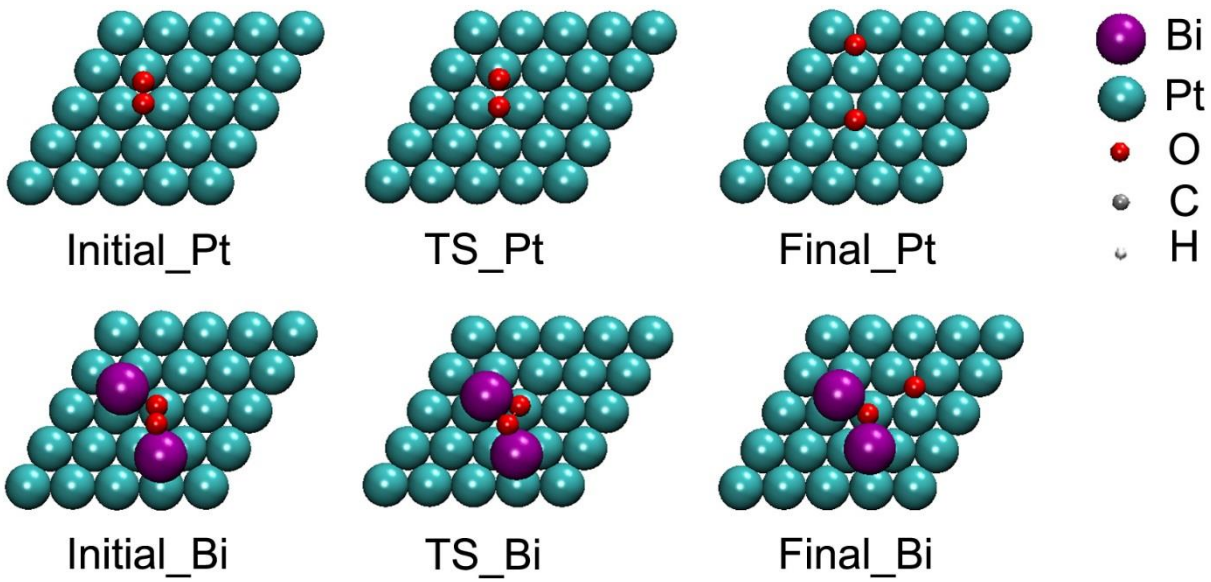


Figure S3. Initial, transition and final geometries of O_2 dissociative adsorption on Pt and Pt-Bi models

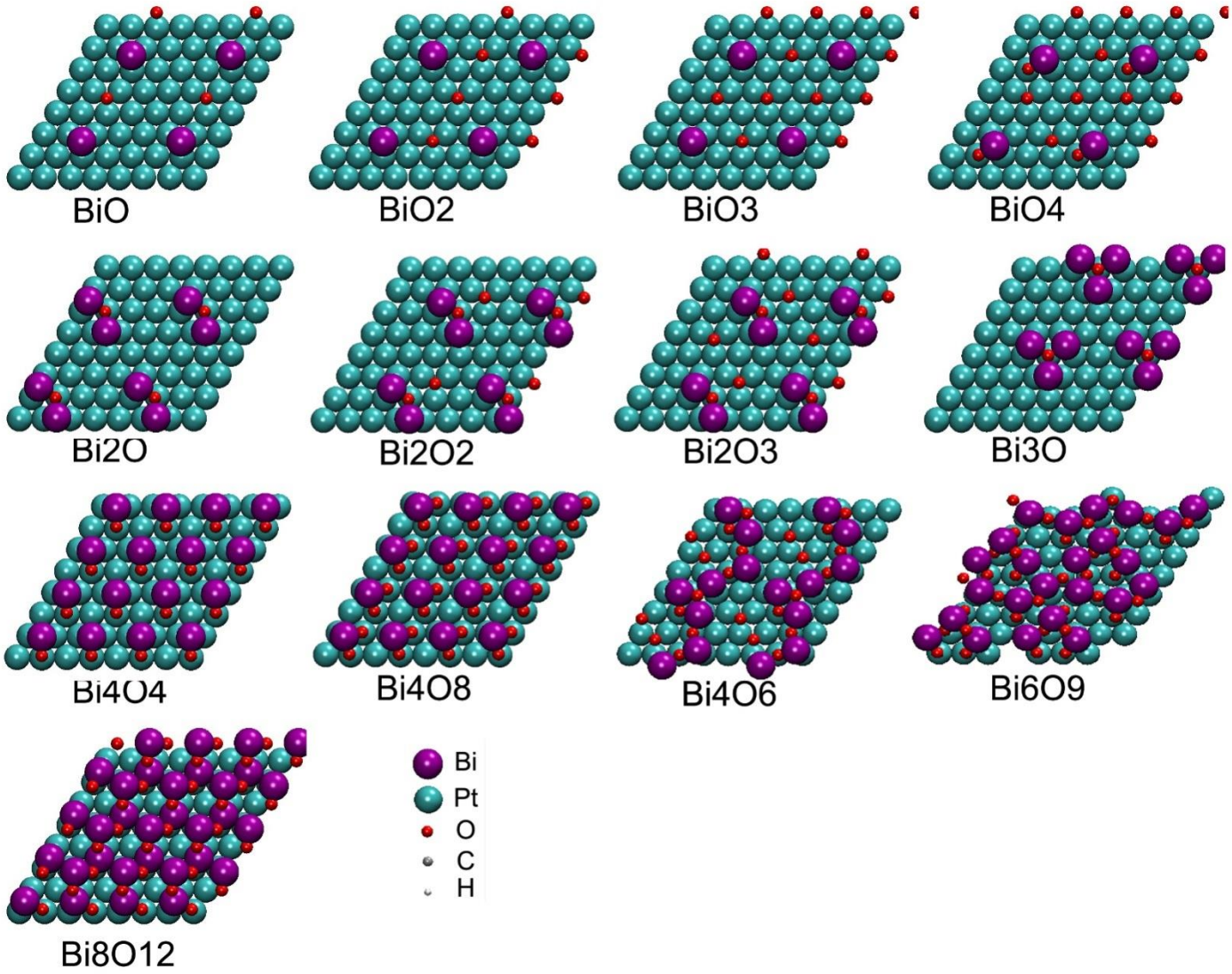


Figure S4. Geometries of different oxidized bismuth models

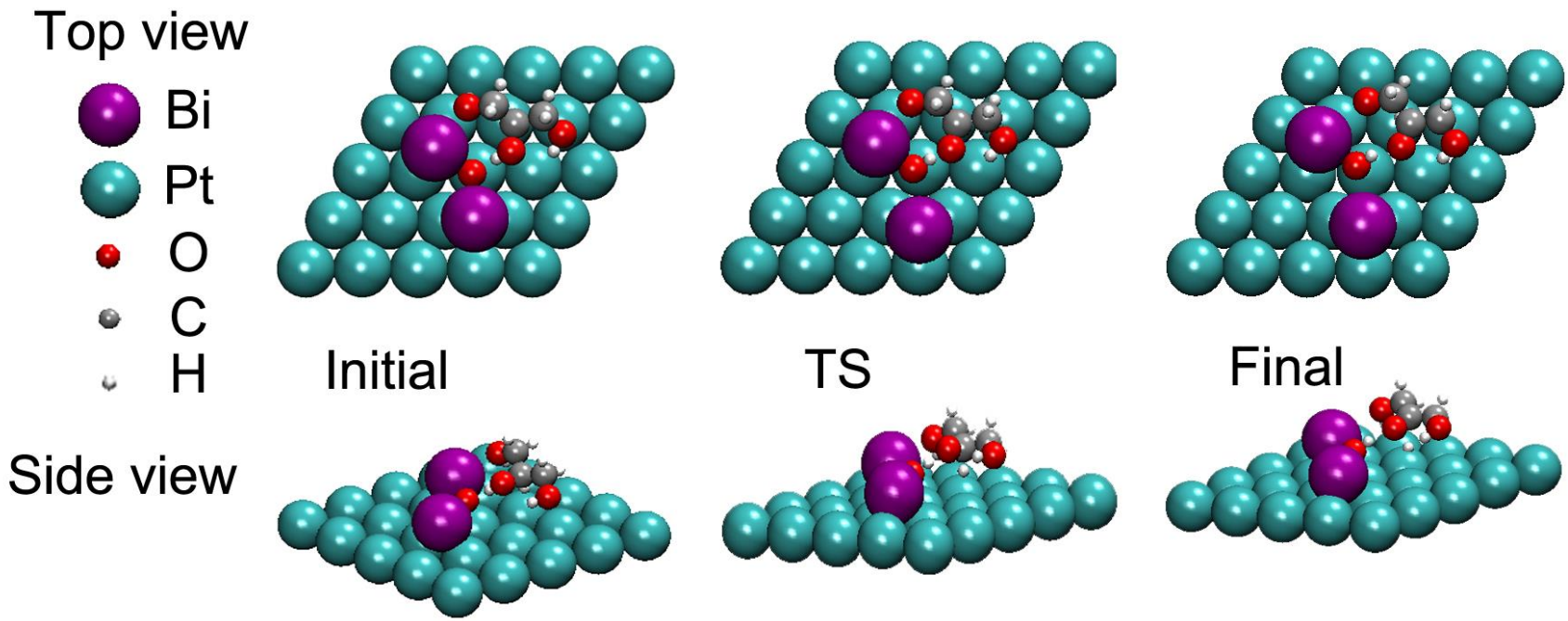


Figure S5. Initial, transition and final geometries of glycerol selective oxidation to DHA on Bi_2O_Pt(111) model.

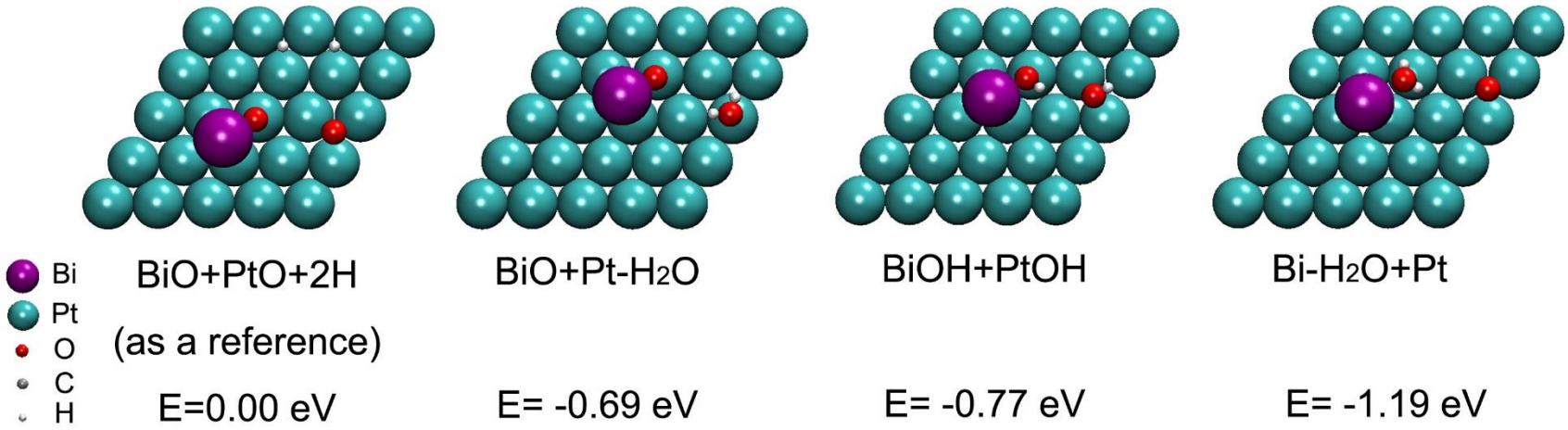


Figure S6. Bismuth site vs Platinum site for H_2O formation

Nomenclature

A	[Å^2]	Area of a given surface
BE	[eV]	Binding energy of an adsorbate
E_a	[eV]	Energy barrier of a given reaction
E_{ad}	[eV]	Energy of a gas molecular adsorbate
$E_{ad/slab}$	[eV]	Energy of a binding adsorbate and a clean slab
E_{IS}	[eV]	Energy of an initial state
E_{slab}	[eV]	Energy of a clean slab
E_{Bi}^{bulk}	[eV]	Energy of an atom in bulk Bi
E_{Pt}^{bulk}	[eV]	Energy of an atom in bulk Pt
E_{TS}	[eV]	Energy of a transition state
G	[eV]	Free Gibbs energy
$g_{Bi_2O_3}^{bulk}$	[eV]	Free Gibbs energy of Bi_2O_3 bulk
g_{Bi}^{bulk}	[eV]	Free Gibbs energy of Bi bulk

k	[J/K]	Boltzmann constant
n_{Bi}	[-]	Number of Bi atoms
n_{Pt}	[-]	Number of Pt atoms
p	[Pa]	Pressure
T	[K]	Temperature
x	[-]	Number of Bi atoms in a Bi_xO_y cluster
y	[-]	Number of O atoms in a Bi_xO_y cluster
μ_{Bi}	[eV]	Bismuth chemical potential;
μ_O	[eV]	Oxygen chemical potential
$\gamma(T,p)$	[eV]	Surface free energy

References

1. Reuter, K.; Scheffler, M. Composition, structure, and stability of RuO2(110) as a function of oxygen pressure. Phys Rev B 2002, 65.
2. Crystallography Open Database, http://www.crystallography.net/.